Review

Richard Mathew Ferguson, Amit P. Khandhar, Hamed Arami, Loc Hua, Ondrej Hovorka and Kannan M. Krishnan*

Tailoring the magnetic and pharmacokinetic properties of iron oxide magnetic particle imaging tracers

Abstract: Magnetic particle imaging (MPI) is an attractive new modality for imaging distributions of iron oxide nanoparticle tracers *in vivo*. With exceptional contrast, high sensitivity, and good spatial resolution, MPI shows promise for clinical imaging in angiography and oncology. Critically, MPI requires high-quality iron oxide nanoparticle tracers with tailored magnetic and surface properties to achieve its full potential. In this review, we discuss optimizing iron oxide nanoparticles' physical, magnetic, and pharmacokinetic properties for MPI, highlighting results from our recent work in which we demonstrated tailored, biocompatible iron oxide nanoparticle tracers that provided two times better linear spatial resolution and five times better signal-to-noise ratio than Resovist.

Keywords: iron oxide nanoparticles; magnetic particle imaging; magnetic relaxation.

***Corresponding author: Kannan M. Krishnan,** Department of Materials Science and Engineering, University of Washington, Box 352120, Seattle, WA 98195, USA, E-mail: kannanmk@uw.edu
Richard Mathew Ferguson, Amit P. Khandhar, Hamed Arami and Loc Hua: Department of Materials Science and Engineering, University of Washington, Box 352120, Seattle, WA 98195, USA
Ondrej Hovorka: Department of Physics, University of York, Heslington, York Y010 5DD, UK

Introduction

Optimized tracers can enhance magnetic particle imaging (MPI) signal-to-noise ratio (SNR) and spatial resolution [13, 16, 19, 25]. In fact, tracers represent the most efficient means of improving MPI performance and may be the key to bringing MPI to the clinic. For clinical applications such as vascular imaging and oncology, tracer magnetism and pharmacokinetics must be optimized to achieve long circulation time, good resolution, and sufficient SNR at safe tracer concentrations and without any adverse side affects. The physical parameters that govern MPI performance are optimized by tailoring tracer magnetic core properties, including size, size distribution, and phase homogeneity, whereas pharmacokinetic properties are tailored with surface chemistry and functionalization to prevent cytotoxicity and ensure desirable biodistribution and circulation time. When designing tracers for clinical MPI application, biocompatibility and performance are both necessary conditions.

Fortunately, iron oxide particles are well tolerated and have a long history of safe application in the clinic [27, 31, 38]. Furthermore, owing to their relatively large magnetic moment and low magnetic anisotropy (cf. "MNP magnetism and MPI"), they are also suited to MPI. To achieve the desired performance and pharmacokinetics, nanoparticle size, uniformity, and surface functionalization must be controlled. In this review, we discuss the key points of MPI tracer design for performance and biocompatibility, emphasizing results from our work.

Magnetic nanoparticle detection in MPI

MPI exploits the non-linear magnetization (Figure 1) of superparamagnetic nanoparticles to generate a localized signal during imaging. A modulating magnetic field, $H(t)$, (typically 25 kHz, 0.02 T/μ_0 amplitude) excites the magnetic nanoparticles (MNPs). The MNP moment, $m(H)$, responds in a non-linear manner, inducing a signal voltage in a receive coil. An additional gradient field, called the selection field, is applied to localize the received signal. The selection field features a field-free point (FFP) surrounded by a gradient of ~2–8 T/μ_0/m, sufficient to saturate the magnetization of MNPs located outside the FFP. Images are formed by scanning the FFP through the sample and recording the MPI signal.

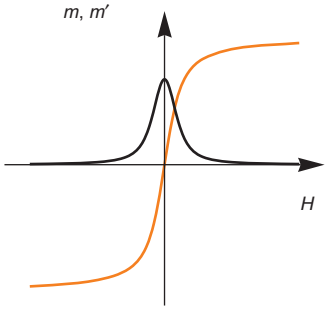

Figure 1 Non-linear magnetization of magnetic particles and the tracer response, $m'(H)$.

Two algorithms are now commonly employed to reconstruct an image from the raw MPI data. System matrix reconstruction [16, 29] is the original MPI method, wherein images are formed by recording the Fourier transform of the received signal and solving the inverse imaging problem using a $N_x N_y N_z N_H N_d$ matrix (called the system function) [29, 30], where there are N_x, N_y, and N_z imaging voxels along the principal directions; N_H is the number of harmonics of the drive frequency that are detected by the N_d independent detectors. While system matrix reconstruction can be very fast [39], it requires that the system function be acquired before the imaging scan, and that the particle response during imaging experiments is the same as during the system function measurement.

In x-space MPI reconstruction [17, 18] the instantaneous MPI signal is assigned to the current FFP location after velocity compensation. The MPI image, which is linear and shift invariant, is now simply a convolution between the MNP distribution and the point spread function (PSF),

$$h(x)=m'(G\cdot x), \tag{1}$$

where G is the gradient strength in $T/\mu_0/m$ and the PSF is assumed to be isotropic over the imaging volume. X-space reconstruction requires no *a priori* knowledge of a system function; however, it is necessary that the FFP position and velocity be well defined at all times during the acquisition scan. If deconvolution is used to improve the displayed image, the PSF should be measured for each tracer formulation.

Whether using system matrix or x-space reconstruction, MPI physics is governed by the tracer response, defined as the derivative of tracer magnetization, $m'(H)$ [m^3], as well as the excitation field slew rate, $G\cdot x_s'$ [$T/\mu_0/s$], where G is the gradient strength [$T/\mu_0/m$] and x_s' the FFP velocity [m/s]. The tracer response is recognized to be a crucial determinant of SNR and spatial resolution. Measurement of the tracer response is critical for tailoring MNPs for MPI; magnetic particle spectrometry, a rapid characterization method for evaluating the tracer response, is discussed in the next section.

Magnetic particle spectrometry

In the absence of MPI scanners, which are currently scarce, an easy-to-construct [13] magnetic particle spectrometer (MPS) [8] provides a means for rapid characterization of MNP performance under magnetic excitation relevant for MPI. (Typically, MPS refers to an instrument designed to measure the Fourier transform, $\mathcal{F}(m')$, of the tracer response, relevant for system matrix reconstruction, while x-space relaxometer [20] refers to an instrument designed to measure the tracer response, $m'(H)$, relevant for x-space reconstruction. (It is possible to measure both with the same instrument [13], as we have done here.) When evaluating tracer performance, a broader spectrum, with higher harmonic intensity, measured by the spectrometer and narrower tracer response (FWHM) measured by the relaxometer indicate superior spatial resolution; intensity per unit iron determines the tracer contribution to SNR for both instruments.

The magnetic field applied by the MPS can be described as

$$H(t)=H_0\sin(\omega t) \tag{2}$$

in which H_0 is the peak excitation amplitude and ω the angular frequency ($2\pi f_0$). The induced voltage, V, is determined by the variation of the MNP tracer's net magnetic moment with applied field, $m(H)$, according to [13, 20, 33]:

$$V(t)=-\mu_0 S(m'(t))=-\mu_0 S(m'(H))(H'(t)) \tag{3}$$

in which μ_0 is the vacuum permeability [$4\pi\times10^{-7}$ Vs/Am] and S is the coil sensitivity [1/m]. Rearranging Eq. (3) yields

$$m'(H(t))=\frac{-1}{\mu_0 S\omega H_0}\cdot\frac{V(t)}{\cos(\omega t)}. \tag{4}$$

Harmonic spectra are generated by Fourier transform of the received signal, $V(t)$. When evaluating candidate MNPs, the tracer response, which has units of m^3, should be scaled by the quantity of iron in the sample to give units of m^3/g Fe. The tracer response is a useful metric for evaluating tracer behavior based only on the applied field and tracer properties. In x-space MPI, the tracer response can be related directly to the PSF [Eq. (1)] when the field gradient, G, is known; the tracer response can therefore be used to predict spatial resolution. However, as will

be discussed in "MNP magnetism and MPI", the tracer response depends on the applied field amplitude and frequency; it is therefore important that the MPS applied field match that used during imaging.

MPI signal linearity

The MPI signal described in the previous section is perfectly linear with MNP concentration in the voxel. This important feature is useful for MPI applications in molecular imaging, cell tracking, etc., as well as potential applications in angiography (measuring artery volume) and oncology (measuring tumor size, vasculature). The signal remains linear provided the tracer MNPs are non-interacting, and remain so (i.e., do not aggregate) *in vivo*. Results of a dilution series, showing signal linearity, are provided in Figure 2.

MNP magnetism and MPI

Magnetic reversal in nanoparticles

In nanoparticles, magnetic behavior is governed by the particle anisotropy [34], which establishes preferred orientations of the magnetic moment within the particle, determines the energy barrier between these orientations and thus the magnetic relaxation dynamics. Furthermore, thermal fluctuations are of critical importance and we will discuss in this section why the thermal energy and anisotropy energies should be similar for MNPs to perform well in MPI. A recent report by Weizenecker et al. [40] uses micromagnetic simulation to emphasize this balance of energies. In that work, shape anisotropy was emphasized, although in practice spin-orbit-lattice coupling (magnetocrystalline anisotropy) and surface effects can also contribute. It is common practice to treat the effective nanoparticle anisotropy as being first-order-dominant uniaxial.

For single-domain MNPs dispersed in solution, the magnetic moment can rotate within the magnetic crystal (the Néel mechanism) or by the physical rotation of the entire nanoparticle (Brown mechanism). One or the other mechanism will typically dominate, as determined by the energy barrier (e.g., the product of the anisotropy constant and the particle volume), thermal energy, viscous drag forces between the MNP and carrier, and the applied field amplitude and frequency. For spinel phase iron oxide MNPs and the applied field conditions typically used in MPI (25 kHz, ~20 mT/μ_0 amplitude), the energy supplied by the applied field is strong enough to reduce the energy barrier created by magnetic anisotropy. Thermal energy also contributes to lowering the energy barrier for rotation of the moment into the direction of the applied field. As a result, the observed relaxation behavior of the nanoparticle tracer depends on the applied field ramping rate.

In this section, we discuss models of magnetic relaxation, and utilize them to interpret MPS experiments performed with different applied field conditions (250 kHz, 25 kHz, and varying field amplitude). We will show that Néel reversal dominates, but as a result of the relatively large field amplitudes employed in most MPI experiments, hysteresis is predicted in $m(H)$ behavior of typical MNPs, with coercivity, H_C, that depends on MNP anisotropy (size) and characteristics of the applied field.

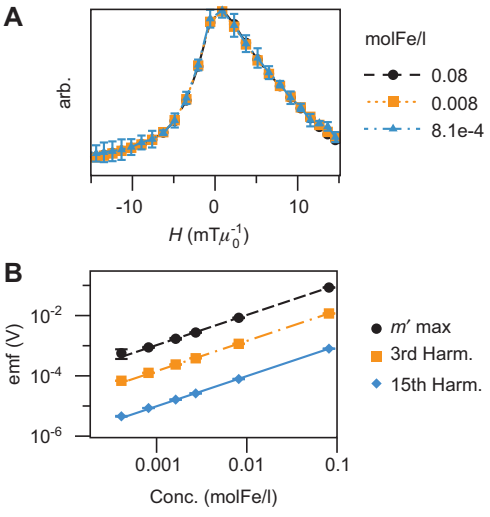

Figure 2 Linearity of MPI signal.
(A) m' of dilutions is constant with decreasing concentration.
(B) Maximum m' and harmonic intensity is linear with concentration.

Néel and Brownian relaxation processes

In nanoparticles, thermal fluctuations compete with magnetic order to determine the MNP response to an applied field. The degree of order is influenced by particle size, as well as measurement time. A particle is blocked when, for a given measurement time, thermal energy is insufficient to surmount the energy barrier established by the particle anisotropy, ensuring that the moment is tied to the anisotropy direction. Thus, the blocking condition is given by

$$\epsilon_B(H=0)=KV>k_BT\log\frac{\tau_{meas}}{\tau_0}, \quad (5)$$

where the anisotropy is assumed to be magnetocrystalline, with K the magnetocrystalline anisotropy constant [J/m^3], V the magnetic volume, k_B Boltzmann's constant, τ_{meas} the measurement time, and τ_0 the attempt time (typically 10^{-10} s).

Superparamagnetism is usually defined for static measurements as the behavior shown by particles smaller than the critical size for blocking when τ_{meas}=100 s [10]. Therefore, according to Eq. (5), the critical size for magnetite is ~28 nm (diameter). The typical time scale, τ_{meas}, in MPI is ~20 µs, or half of the period of the commonly used 25 kHz excitation field. In this case, the critical size is smaller, about ~21 nm (diameter) for magnetite particles. In both calculations, we have assumed that K=11 kJ/m^3, the value for bulk magnetite [10].

For spherical, non-interacting particles subject to an applied field, the energy barrier due to an effective uniaxial magnetocrystalline anisotropy is

$$\epsilon_B(H)=KV\left(1-\frac{H}{H_K}\right)^2=KV\left(1-\frac{\mu_0 M_s H}{2K}\right)^2, \quad (6)$$

where μ_0 is $4\pi\times10^{-7}$ [Vs/Am], M_s is the volume saturation magnetization [A/m], and H is the magnetic field [T/μ_0] applied parallel to the anisotropy axis. When H is large, the particle moment prefers to align parallel to the field, causing the energy barrier for rotation into alignment to shrink and ultimately disappear as the moment is forced into the parallel orientation at the critical field, H_K ($2K/\mu_0 M_s$).

The Néel relaxation time, τ_N, describes reversal of the magnetic moment vector within the magnetic crystal itself, without any physical motion of the particle. In the absence of an applied field, thermal fluctuations can allow the moment to hop over the energy barrier. In the presence of an applied field, the energy barrier is modified, increasing the probability of hopping from the antiparallel to parallel state. Combining and rearranging Eqs. (5) and (6), the Néel relaxation time can be written as

$$\tau_N=\tau_0*\exp\left(\frac{KV*\left(1-\frac{H}{H_K}\right)^2}{k_bT}\right). \quad (7)$$

Example times, calculated from Eq. (7) for magnetite particles subject to increasing applied field strengths, are plotted in Figure 3. The anisotropy constant, K, was assumed to be the bulk value, i.e., K=11 kJ/m^3. The application of a 10 mT/μ_0 field significantly shortens the Néel relaxation time (Figure 3A). For 30-nm magnetite particles, it reduces τ_N by ~8 orders of magnitude. Owing to exponential dependence on magnetic volume, V, τ_N ranges from nanoseconds to days for the range of diameters between 10 and 30 nm in the absence of an applied field (Figure 3B). Exponential dependence on anisotropy leads to similar variation. Anisotropy can vary owing to surface/volume effects due to size as well as the shape of the nanoparticles, and from variations in crystalline structure between different materials.

For particles in solution, magnetic relaxation can also occur by physical rotation of the particle (i.e., rotation of the anisotropy axis) at a rate that is governed by random collisions with molecules in solution. By this mechanism, called Brownian relaxation, blocked particles can relax faster than τ_N, provided they are able to move freely. The Brownian rotational diffusion time constant is [15, 34]

$$\tau_B=\frac{3V_H\eta}{k_BT}=\frac{\pi d_H^3\eta}{2k_BT}, \quad (8)$$

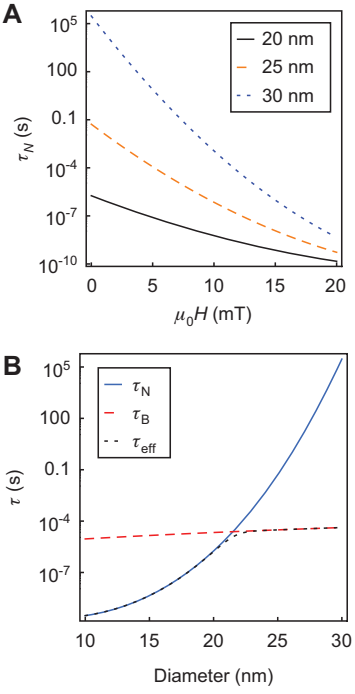

Figure 3 Magnetic relaxation times.
(A) Néel relaxation time calculated using Eq. (7) for magnetite nanoparticles with different diameters, under applied fields of increasing strength. Magnetocrystalline anisotropy with K=11 kJ/m^3 was assumed. (B) Relaxation times calculated for H=0 according to Eqs. (7)–(9). For calculations, the hydrodynamic layer thickness, δ, was assumed to be 10 nm, and the magnetocrystalline anisotropy, K, was the bulk value, 11 kJ/m^3.

where η is the fluid viscosity and d_H is the hydrodynamic diameter. We note that τ_B in Eq. (8) is defined for small angles of rotation and small fields ($H<<H_K$), so that field amplitude is neglected. For the ~20 μs time scale typical in MPI, the critical hydrodynamic size for Brownian relaxation is 39 nm diameter; according to Eq. (8), anything larger will not show Brownian relaxation within the time limit defined by the MPI instrument. For weak applied fields, the faster of the two relaxation times will dominate, such that the effective time is

$$\tau_{eff} = \frac{\tau_N \tau_B}{\tau_N + \tau_B}. \quad (9)$$

Generally, for unblocked particles, the Néel mechanism will dominate, although it is important to note that for blocked particles, Brownian and Néel relaxation modes compete, with the fastest mode dominating. However, it can be challenging to determine the active mode in practice. Properties of the MNPs, their environment, and the applied field must be considered: carrier fluid viscosity, magnetic domain size, anisotropy energy barrier, particle hydrodynamic size, applied field frequency, and amplitude each influences the active mode. For example, the Brownian relaxation time of nanoparticles will change significantly *in vivo* if the nanoparticles are opsonized by plasma proteins, or could be prevented entirely by binding to tissue. More discussion of *in vivo* particokinetics follows in the section "Synthesis of biocompatible iron oxide particles tailored for MPI: performance, pharmacokinetics, biodistribution, circulation, and clearance". It is also possible that multiple modes can be active simultaneously if there is a distribution of MNP sizes or compositions. For magnetically blocked particles with small hydrodynamic size subject to small fields, Brownian relaxation will typically dominate, while for larger fields, comparable to H_K, such as those used in MPI, or if MNPs are bound such that they cannot physically rotate, Néel processes will dominate.

For iron oxide MNPs tailored for MPI performance in our laboratories, the Néel reversal mechanism dominates under typical conditions (15–27 nm core diameter MNPs, 25 kHz, 20 mT/μ_0). We emphasize that, under these conditions $H<<H_K$ is not satisfied and the moment of such iron oxide particles will be driven to reverse by the applied field through the Néel process. As a result, according to Eq. (7), in a strong enough field, the Néel relaxation time is quite short even for MNPs larger than ~19 nm, which would be blocked in the absence of an applied field. Field-driven reversal leads to the appearance of hysteresis in the *M-H* loops measured by MPS. (However, no hysteresis is measured during room temperature *M-H* measurements of the same MNPs by VSM, where the ramping rate is slow.) A model of MNP magnetization that accounts for the field-driven reversal under typical conditions and shows good agreement with measured results is described in "Modeling MNP magnetization in response to alternating fields". Finally, we note that Brownian relaxation could play a role in aligning the anisotropy axes of the nanoparticles in solution and thereby have some impact on the system's magnetic response; the extent of this role should be investigated in future work.

A simple experiment was designed to evaluate the relative contributions of Néel and Brownian/viscous relaxation to the MPI process: MNPs were dispersed in water and immobilized in agarose gel and their MPS signal was measured.

Experimental: MPS evaluation of mobile and immobilized tracers

MNPs with magnetic core size of d_0=23 nm were selected, as magnetite MNPs of this size with typical magnetic anisotropy (K=11 kJ/m^3) are expected to be blocked at standard MPI conditions of 25 kHz, 20 mT/μ_0 applied field. Magnetic size distributions for this sample and all others mentioned in this work were determined by fitting to room temperature $m(H)$ curves measured by vibrating sample magnetometer [14]. A log-normal distribution of the form

$$g(d_c) = \frac{1}{\sigma * d_c * \sqrt{2*\pi}} \exp - \frac{\left(\ln\left(\frac{d_c}{d_0}\right)\right)^2}{2*\sigma^2} \quad (10)$$

was assumed, with d_c the magnetic core diameter, d_0 the median core diameter, and σ the standard deviation of the distribution.

The sample was dispersed in water following standard coating with PMAO-5 kDa molecular weight poly(ethylene glycol) (PEG) (see "Synthesis of biocompatible iron oxide particles tailored for MPI: performance, pharmacokinetics, biodistribution, circulation, and clearance" for discussion, and ref. [24] for experimental details). The hydrodynamic size, d_H, of the water-dispersed tracer was 58 nm. The same MNPs were dispersed in a 1 wt% agarose gel. Equal parts of MNP solution and 2% agarose solution in water were combined at 90°C to make the sample, which was allowed to cool and solidify before measurement.

MPS measurements, acquired using the UW system [13] at 25 kHz, 20 mT/μ_0, are provided in Figure 4.

The hysteresis loop (Figure 4A) was obtained by integrating the measured tracer response [$m'(H)$, Eq. (4)], shown in Figure 4B. The harmonic spectrum, calculated from $m'(t)$, is shown in Figure 4C.

Despite the change in viscosity between water and the solid gel, very little change was observed in the tracer response or harmonic spectrum. Error bars in Figure 4B show the standard deviation of three measurements made for each sample (for visual clarity, the error bars are shown only for the ascending branch). There are some slight differences, although the measurement errors overlap almost completely, indicating that the magnetic reversal had negligible dependence on Brownian rotation. We can conclude that the magnetic moment must have rotated within the crystal itself through the Néel process. Importantly, hysteresis in $m(H)$ and $m'(H)$ indicates that the MNPs were blocked during the experiment and that the applied field contributed significantly to the magnetic reversal energy.

Slight differences in the $m(H)$ loops near the edges of the field of view may be due to a small contribution from Brownian rotation, which enables the anisotropy axes of the particle to fully align in water. Such alignment should be prevented in the gel and could explain the observed difference. The pore size of 1 wt% agarose gel was measured by previous researchers to be approximately 200 nm [28], of the order of the hydrodynamic size of the magnetic particles (~60 nm). While further investigation is needed to determine precisely how the MNPs behave within the gel pores and to what extent they locally wiggle [41], there is sufficient change in sample morphology from water to gel that we would expect a measureable change in response if Brownian reversal were the dominant mode.

MPS measurements of the gelled sample were obtained with varying applied field amplitude while holding the frequency constant. The results are shown in Figure 5. For 10 and 5 mT/μ_0 excitation, only minor $m(H)$ loops (Figure 5A) are excited, although the maximum in $m'(H)$ (Figure 5B) remains constant with changing amplitude. Harmonic intensity was calculated from measured $V(t)$. Spectra were normalized by the first term in Eq. (4), $\frac{1}{S\omega\mu_0 H_0}$, so that the variations in field ramping rate did not influence the spectral intensity. Spectral intensities were constant for the complete loops (H>15 mT), but decreased when only a minor loop was excited by the lower drive fields.

Experiments like the one described here illustrate the importance of understanding how MNP anisotropy influences the MPI response. The simple model of Néel relaxation time given in Eq. (7) provides a basic description of the reversal process, including the response to a continuous, instantaneously applied field. However, more sophisticated models are needed to model the MNP response to continuously varying fields typically used in MPI. In the next section, we describe such a model and compare it with experiments. Subsequently, we discuss tracer performance at different applied field strengths and frequencies.

Modeling MNP magnetization in response to alternating fields

When blocked MNPs are subject to an alternating field of sufficient amplitude to shorten their Néel relaxation time, hysteresis appears in the $m(H)$ loop. Modeling the MNP response can be complex and typically requires numerical methods [9, 36]. Recently, a model was presented that uses a stochastic differential equation to model the MNP response during MPI as a function of particle anisotropy and applied field conditions, with thermal fluctuations modeled as a randomly fluctuating field [40]. We are developing a model that uses a kinetic Monte Carlo method to introduce thermal fluctuations to the Stoner-Wohlfarth model. In this section, we discuss ferromagnetic behavior

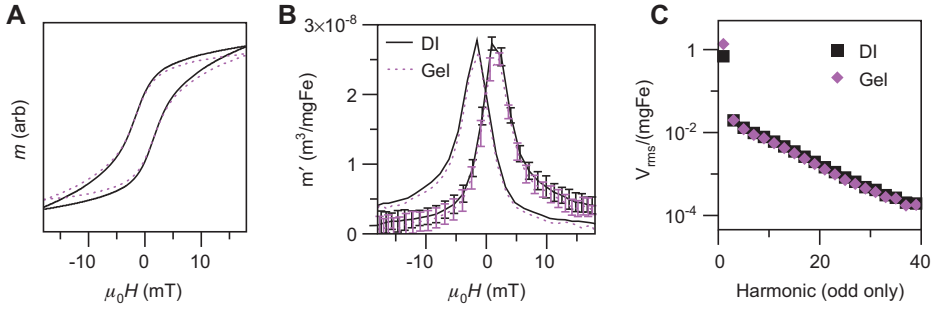

Figure 4 MPS results of water and gel samples.
(A) $m(H)$ curves integrated from measured tracer response (B) of 23 nm (d_0, σ=0.28, hydrodynamic diameter, d_H=58 nm) MNPs dispersed in water and immobilized in 1 wt% agarose gel. The hydrodynamic diameter was (C) harmonic spectrum measured by MPS.

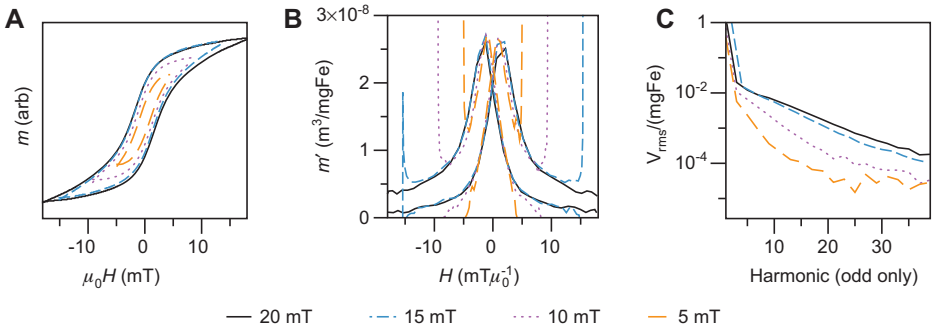

Figure 5 MPS response to changing field amplitude.
(A) *M-H* loop, calculated by integrating the measured tracer response (B). (C) Harmonic spectrum of a gelled MNP sample subjected to varying field amplitude. d_0 was 23 nm, d_H was 58 nm.

of single-domain MNPs when thermal fluctuations are present, then briefly describe the model and provide some preliminary results.

The Stoner-Wohlfarth model [35] describes the magnetic response of single-domain ferromagnetic particles with general anisotropy. However, the Stoner-Wohlfarth model considers only the anisotropy and Zeeman energies in determining the moment orientation, so while it is valid for all domain sizes at T=0, it should be modified to include thermal fluctuations when T>0, in particular for particles with small energy barriers. Thermal fluctuations have the effect of reducing the coercivity, H_C, proportionally with the energy barrier, $K_{eff}V$. Coercivity also depends on the driving field amplitude and frequency (i.e., ramping rate). For the case of the field applied along the easy axis of magnetization, the coercivity is given by [9]

$$\mu_0 H_C = \mu_0 H_K \left(1-k^{\frac{1}{2}}\right), \tag{11}$$

where

$$k = \frac{k_B T}{K_{eff} V} \ln\left(\frac{k_B T}{4\mu_0 H_{max} M_S V_f \tau_0}\right), \tag{12}$$

with H_K the field at which the energy barrier due to general uniaxial anisotropy is suppressed (equal to $\frac{2K}{\mu_0 M_s}$ for magnetocrystalline anisotropy, where K is the magnetocrystalline anisotropy constant), K_{eff} is the effective uniaxial anisotropy, and V is the particle volume. For a random orientation of particles, the coercive field is given by [9]

$$\mu_0 H_C = 0.48\, \mu_0 H_K (b-k^n). \tag{13}$$

where b=1 and n~0.8. It is important to note that the applied field ramping rate influences the coercivity: when more time is permitted for thermal hopping over the barrier, i.e., for slower ramping rates, the coercivity is reduced, while for faster ramping rates the coercivity is greater. Coercivities were calculated using Eq. (13) for particles of varying size and anisotropy, and the results are shown in Figure 6B.

To simulate tracer magnetization in relevant driving field conditions, we are developing a numerical model that combines the Stoner-Wohlfarth theory of coherent rotation with a kinetic Monte Carlo method to introduce thermal fluctuations in the moment vector orientation [21]. The model calculates the orientation of the magnetic moment for each particle in a collection of 2000 particles

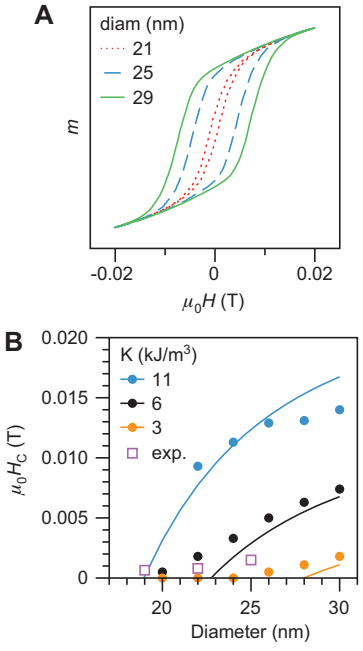

Figure 6 Simulated magnetic behavior.
(A) *M-H* loops calculated for randomly oriented, monodisperse particles where K=11 kJ/m³. (B) $H_C(d)$ for K [kJ/m³]=11, K=6, and K=3 calculated using Eq. (3) (sold lines), and from Monte Carlo simulations (dots). Open squares were measured for samples of the specified median diameter under 25 kHz, 20 mT/μ_0 applied field.

with randomly oriented anisotropy axes, which are fixed (i.e., no Brownian rotation is permitted). Particle anisotropy is modeled with an effective uniaxial anisotropy term,

$$K_{\text{eff}} = K_1 + K_M = K_1 + \frac{\mu_0 M_s^2}{2}(N_\perp - N_\parallel) \quad (14)$$

that contains uniaxial magnetocrystalline (K_1) and shape anisotropy (K_M) terms (in this work, we have neglected the shape anisotropy, which is appropriate considering the isotropic shape of our synthesized nanoparticles). According to the Stoner-Wohlfarth model, the energy of the system, E', is determined by the anisotropy and Zeeman energies [35],

$$E' = E_K + E_H = V[K_{\text{eff}}\sin^2(\theta) - \mu_0 M_s H_a \cos(\theta - \theta_H)], \quad (15)$$

H_a is the applied field, θ is the angle between the anisotropy axis and the magnetic moment, and θ_H, is the angle between the anisotropy axis and the applied field. For a given orientation of the particle anisotropy and applied field, the minimum energy of the system, and thus the orientation of the particle moment at thermal equilibrium, can be determined from Eq. (15). For example, in the absence of an applied field, there are two equivalent energy minima: θ=0, the "+" state, and θ=π, the "-" state. Given some initial orientation of the moment, the transition rates, $w\pm$, between the states are given by [7]

$$w_\pm = \frac{1}{\tau_0}\exp\left(\frac{\Delta G_\pm}{k_B T}\right), \quad (16)$$

where $\Delta G_\pm$ are the two energy barriers between the up and down states determined by Eq. (15). In our model, the orientation of the applied field is divided into discrete time steps, and the moment is calculated at each time step of the applied field using kinetic Monte Carlo governed by the transition rates given in Eq. (16).

We used the model to calculate hysteresis loops at 25 kHz, 20 mT/μ_0 field conditions common in MPI. Results for K=11 kJ/m^3 are shown in Figure 6A. The model predicts the appearance of hysteresis in $m(H)$ measurements for particles >20 nm, with coercivity that increases with particle size. The differential susceptibility, dM/dH, does not increase significantly with particle size once the $m(H)$ loop has opened. In fact, when particles are monodisperse, maximum susceptibility occurs just as the loop begins to open, followed by a reduction of 5–10%. Note that this contradicts Langevin theory, which predicts a monotonic increase in susceptibility with increasing particle volume. Therefore, the Langevin model is not the best theory for MPI under commonly used conditions for particles larger than ~20 nm diameter (actual size depends on the anisotropy particular to a given sample).

The importance of minimizing size distribution is apparent when one considers that mixing sizes creates an effective $m'(H)$ response with a broader peak, due to the mix of coercivities present in the sample. This has the effect of reducing the received MPI signal, per unit iron, and broadening the spatial resolution of the native MPI tracer response.

We have approached MPI tracer optimization by focusing on synthesizing highly uniform single-core MNPs with size and shape (and therefore anisotropy) tuned to maximize response for the driving frequency of interest. However, in addition to magnetic core properties, properties of the surface must also be optimized to ensure stability of the magnetic core *in vivo*. In the next section, we discuss methods for synthesizing tailored, biocompatible MPI tracers, as well as some *in vivo* and *in vitro* experimental results.

Synthesis of biocompatible iron oxide particles tailored for MPI: performance, pharmacokinetics, biodistribution, circulation, and clearance

Tailored magnetic behavior is essential for MPI performance, as discussed in "MNP magnetism and MPI". Thermal decomposition reactions are an effective approach to controlling MNP size, size distribution, phase purity, and their resulting magnetic properties [13]. Phase transfer protocols should protect tailored behavior by minimizing cluster formation during addition of a biocompatible shell to the MNPs. The polymer shell composition should also be tailored to achieve the needed hydrodynamic size for *in vivo* stability and favorable circulation, biodistribution, and whole body clearance [23].

In this section, we discuss magnetic core synthesis reactions, emphasizing the importance of size (and shape) control. We also discuss surface modification to ensure that particles are stable *in vivo*, with favorable pharmacokinetics. Examples are provided from recent results of MPS measurements of tailored tracers *in vitro* and preliminary circulation time and biodistribution measurements of tailored tracer.

Synthesis of tailored iron oxide MNPs

Iron oxide MNPs are biocompatible and biodegradable, and several formulations have previously been approved clinically safe by the Food and Drug Administration [27, 31]. Furthermore, the magnetite and maghemite phases are suited to MPI physics, with relatively large saturation magnetization and small magnetic anisotropy. Generally, there are two major approaches for preparation of iron oxide nanoparticles: coprecipitation and thermal decomposition.

Conventionally, iron oxide MNPs were prepared from coprecipitation of Fe^{2+} and Fe^{3+} ions by addition of an alkaline solution (such as NaOH or NH_4OH). To make the MNPs stable in aqueous media, the synthesis is usually done in the presence of polymer molecules with proper molar ratio [6]. Coprecipitation synthesis has been extensively investigated using different types of polysaccharides, such as dextran [37], chitosan [6], and starch [22]. This method is cheap and scalable, and MNPs are biocompatible without any further processing. However, coprecipitation synthesis provides little control over the magnetic core size, and samples usually have broad size distributions owing to continuous nucleation and growth of the MNPs during the synthesis. Furthermore, magnetic clusters that contain multiple, magnetically coupled MNPs can be produced during synthesis. Clusters have different magnetic behavior than the smaller, single MNPs. When clusters of varying size and polydisperse single MNPs are produced together, as in coprecipitation methods, the resulting MPI response is suboptimal. For example, the MPI signal observed from Resovist, a most commonly used MPI tracer in the preliminary evaluation of this technique, was only 3% of the signal predicted by theory for uniformly sized MNPs with the same iron content [16]. Note that clusters are not necessarily undesirable. For example, in the case of Resovist, clusters provide the desirable part of the response [12]. Recently, investigators produced, through fractionation, nanoparticle solutions that contained appropriately sized clusters in greater concentration and yielded an improved MPS response [26]. We point out that with this approach, it is critical that cluster size be both uniform and tailored to maximize MPI response.

In an alternative approach that is employed in our work, iron oxide MNPs are synthesized by thermal decomposition of iron organometallic complexes such as iron oleate or iron pentacarbonyl. Burst nucleation and uniform growth of the nuclei at high temperatures (e.g., 320°C) and in the presence of surfactants (i.e., oleic acid and/or oleyl amine) results in excellent size and shape uniformity of these MNPs (cf. Figure 7), with core size that can be tuned by adjusting the precursor-to-surfactant ratio and synthesis time and temperature. Synthesized MNPs are phase-pure magnetite, as measured by monochromatic electron energy loss spectroscopy and Raman spectroscopy (data not shown). Using this approach, we have shown that the size of the MNPs can be uniformly controlled from 7 to 27 nm by changing the molar ratio of iron oleate to oleic acid [5, 14, 24]. We can therefore tune the MNP magnetic response to maximize MPI performance, based on the principles described in "MNP magnetism and MPI". However, the major challenge in this method is that the as-synthesized MNPs are coated with hydrophobic ligands and their surface must be modified with additional hydrophilic molecules to make them water soluble and biocompatible. Surface modification adds greater complexity than single step coprecipitation reactions, but robust methods are available.

Various methods have been introduced for phase transfer of hydrophobic MNPs made by thermal decomposition reactions. Ligand exchange is a commonly used approach, in which the oleic acid molecules are replaced by, for example, a hydrophilic silane terminated molecule [4]. Also, some amphiphilic copolymers (e.g., PMAO-PEG) favor a hydrophobic-hydrophobic interaction with the oleic acid molecules on the surface of the as-synthesized MNPs and can be used efficiently as an additional coating layer, making the MNPs highly water soluble.

While the coating process can influence magnetic properties, it primarily determines the MNP's pharmacokinetic properties, such as circulation, biodistribution, and clearance. The coating determines size and size stability in blood by modulating adsorption of plasma proteins to the MNPs. PEG and its derivatives are clinically approved for a wide range of biomedical applications, and furthermore PEG has an antifouling property that in combination with its steric hindrance makes the coated MNPs highly stable during *in vivo* applications. Therefore, it seems to be a proper choice for preparation of the first generation of the MPI tracers with long-term size stability and consistent signal.

Experimental: MPS evaluation of biocompatible, tailored MNPs

MNPs were synthesized with core sizes tailored for MPI performance following the physical principals discussed in previous sections. Prepared by our standard methods, including coating with a 5-kDa molecular weight PEG shell, tracers of ~22–25 nm magnetic core diameter typically show strong MPI performance. An example is shown in Figure 7. Bright field transmission electron

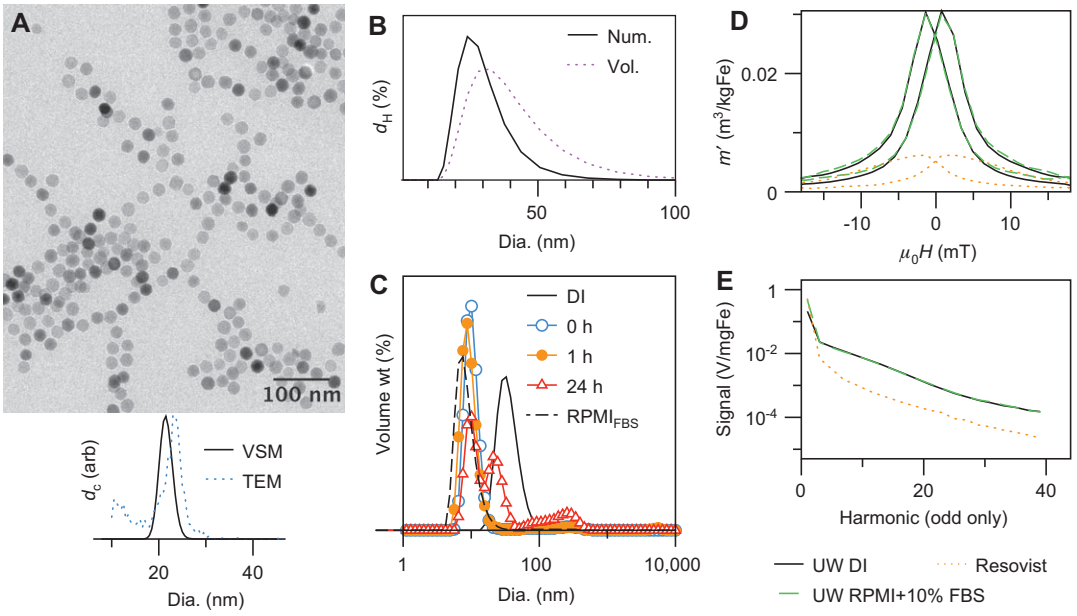

Figure 7 Characterization of a tailored MPI tracer produced at UW.
(A) TEM image of nanoparticles and core size measurements: median magnetic core size, d_0, was 22 nm measured by fitting to $m(H)$ measurements, and 24 nm by TEM. (B) Hydrodynamic diameter, d_H, was 30 nm (mode, volume distribution) measured by DLS. Number and volume-weighted hydrodynamic size distributions are shown. (C) Hydrodynamic size measurements (DLS) in RPMI cell culture media that contained 10% FBS. In media, the nanoparticle size peak is overwhelmed by the serum protein peak (dashed line). After 24 h, the protein peak shrinks and aggregate particles begin to appear, suggesting that the nanoparticles have begun to absorb proteins from the solution. (D, E) MPS measured for UW tracer and Resovist in water, and for UW tracer *in vitro*. UW tracer was measured in cell culture media (RPMI) that contained 10% FBS. Displayed data was measured at 0-h time point.

microscopy (TEM) and size characterization measurements are provided in Figure 7A. Magnetic core size was narrowly distributed (d_0=22 nm, σ=0.2) and results of TEM and $m(H)$ characterization are typically similar, with TEM size often a few nanometers larger. Hydrodynamic size (30 nm, volume distribution mode) is typically 10–20 nm greater than the magnetic core size. The sample showed good long-term stability in biological media, based on MPS measurements and measurements of hydrodynamic size over the course of 24 h (Figure 7C). Dynamic light scattering (DLS) measurements of media with serum only (no nanoparticles) showed a strong peak at ~10 nm, which can be attributed to serum proteins. When nanoparticles were dispersed in media (50% by volume), the protein peak overwhelmed the nanoparticle signal for early time points. After 24 h, the protein peak shrank, indicating that the nanoparticles had begun to adsorb proteins, while at the same time the nanoparticle peak returned due to the lower concentration of proteins. A new peak at ~300 nm appeared, indicating some aggregation of nanoparticles and proteins. The relative frequency of the aggregates was small and is visible only in the volume distribution, which is weighted toward larger sizes.

MPS measurements are provided in Figure 7D, E. Experimental conditions were 25 kHz, H_{max}=20 mT/μ_0. Forward (low to high field) and reverse (high to low field) scans are shown, and the reverse scans are plotted with dimmed color. Signal intensity, measured by the max, of UW tracer was 0.03 m^3/kg Fe, 5× greater than Resovist (0.006 m^3/kg Fe). Resolution, as determined by the tracer response FWHM, was 6.7 mT/μ_0 for the UW tracer, 0.5× that of Resovist (13.7 mT/μ_0). The UW tracer showed greater harmonic intensity for all harmonics: 3.3×, 7.4×, and 6.7× greater at the 3rd, 19th, and 39th harmonics, respectively.

MPS performance was also measured after dispersing the tracer in cell culture media that contained serum proteins [10% fetal bovine serum (FBS)]. The polymer shell plays an important role in protecting the MNP magnetic core from agglomeration due to serum protein adsorption. If the MNPs become unstable and agglomerate, their magnetic behavior can change owing to dipole-dipole interactions within the aggregates, leading to suboptimal behavior. Here, the MPS response showed no change after adding serum (Figure 7D, E). Although not shown, the measured MPS response was unchanged over 24 h in the serum.

Biodistribution, circulation, and clearance

Biocompatibility and performance are equally important in MPI tracers. To translate tailored behavior of tuned MNP magnetic cores *in vivo*, the MNP shell – in addition to rendering the MNPs biocompatible and safe – must play two important roles: (1) demonstrate maximum bioavailability (blood half-life) and (2) protect the magnetic core's optimal MPI performance in the physiological environment. In this section, we will focus on MNP pharmacokinetics and its relevance to clinical translation of MPI.

Our models and experimental results suggest that the optimal core diameter for imaging in a 25-kHz drive field is ~25 nm. However, preexisting physiological upper and lower limits set by the sinusoidal capillaries of the liver and spleen (50–180 nm), which together comprise the reticuloendothelial system (RES), and the kidney fenestrae (~10–15 nm) [32], suggest that MNPs between 15 and 50 nm (hydrodynamic diameter) may prove optimal for long circulation times. However, defining the optimal physical conditions for long-circulating nanoparticles is rather complex and depends on multiple factors, including hydrodynamic diameter, surface coating, surface charge, and, to some extent, the core size as well [1, 3]. For instance, PEG-coated MNPs up to 140–160 nm in hydrodynamic diameter have been shown to circulate for several hours in a rodent model [11]. Furthermore, surface charge is critical; coatings with a neutral or negative surface charge are preferred as a positive surface charge often induces undesirable immune responses that result in rapid removal of MNPs from circulation [1–3]. Among neutral coatings, dextran and PEG-based surface coatings are the most widely used [3]; indeed, several preclinical and clinical iron oxide formulations are coated with either dextran or PEG.

Experimental: circulation and biodistribution

Here we summarize results of blood circulation and biodistribution studies of MPI-tailored MNPs [23]. In the circulation study, we compared our monodisperse PEG-coated MNPs with carboxydextran-coated Resovist MNPs (see Table 1) in female CD-1 mice. Furthermore, results of a pilot biodistribution assessment that investigated the organ distribution and the potential clearance mechanism of two monodisperse MNP formulations in mice, using T2-weighted MRI, are presented. All animal protocols were approved by University of Washington's Institutional Animal Care and Use Committee.

Table 1 Characterization data of UW-17 and Resovist MNPs.

	d_0 (nm) (σ)[a]		d_H (nm)	M_s (kA/m)	MPS	
	VSM	TEM			Signal (V/mg Fe)	W_{FWHM}
UW-17	17 (0.20)	19 (0.15)	86	416 (±27)	0.102	9.9
Resovist	14 (0.47)	5 (0.37)[b]	72	300 (±34)	0.048	12.4

[a]σ is the standard deviation of the log-normal distribution.
[b]TEM characterization data from ref. [35], which provides extensive characterization of Resovist.

Methods

Circulation study

Female CD-1 mice (8 weeks old) were injected with 100 µl of 2.0 g Fe/l MNPs dispersed in 1× PBS through the tail vein. Approximately 100 µl of blood was collected retro-orbitally at two time points from each mouse; mice were euthanized after the second blood draw. As each mouse provided two time points, the study was repeated three times per formulation for statistical relevance; consequently, a total of 15 mice (five mice/trial×three trials) were used per formulation. Similar data sets were obtained for the control and Resovist groups, which were injected with 100 µl 1× PBS and 2.0 g Fe/l Resovist solution, respectively. Blood samples were characterized in our 25 kHz MPS (H=18 mT/μ_0 amplitude) to demonstrate relevance with clinical applications of MPI. The MPS signal is linear with concentration (cf. "MPI signal linearity"), but each MNP formulation must be calibrated. Calibration was performed using a series of MNP dilutions. Iron concentration was measured using inductively coupled plasma-optical emission spectrophotometer (ICP-OES; Perken Elmer, Waltham, MA, USA), and maximum m' was measured in the MPS for each dilution. Whole blood samples (100 µl), extracted at various time points after tail vein injections, were transferred in 0.5-ml Eppendorf tubes and measured directly in the MPS; no processing steps were necessary.

Biodistribution study

To study the dependence of hydrodynamic size on biodistribution and clearance of MNPs, we tested two formulations (see Table 2). For statistical significance, three mice

Table 2 Properties of the two formulations tested in mice for biodistribution and clearance.

Formulation	d_0 (nm)	d_H (nm)	r2 (mM/s)
A	17	86	209
B	19	37	435

per formulation were administered, through the tail vein, with either formulation A or B at 2.5 mg Fe/kg. Control mice (quantity 3) were injected with 100 µl 1× PBS. Mice were anesthetized using 5% isoflurane and maintained at 1–2% during imaging in the 14-T MRI (Bruker Biospin, MRI, Ettlingen, DE). Respiration rate was monitored and maintained between 100 and 150 breaths/min. To acquire reference scans, all mice were imaged before injection. After injection, mice were imaged at 0.5-, 1-, and 24-h time points. All mice were euthanized past the 24-h endpoint.

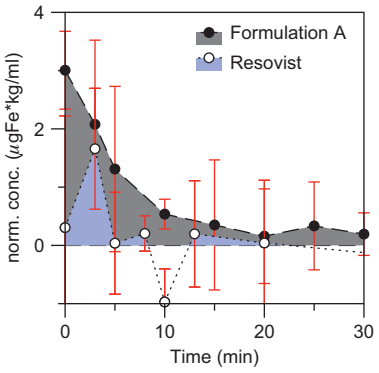

Figure 8 Blood-circulation time of formulation A and Resovist MNPs in female CD-1 mice.
Blood samples were taken from retro-orbital bleeds, and MPS measurements of whole blood samples were used to determine MNP concentration at the specified time points. Error bars are the standard deviation of three blood samples (one per mouse) for each time point.

Results and discussion

Circulation study

Figure 8 compares the circulation time of Resovist with UW MNPs (formulation A, which contained monodisperse 17-nm MNPs). The MNP concentration in blood was quantified using the same signal that would be used for imaging; thus, the results directly correlate with the useful MPI signal. The blood half-life of formulation A – determined using a one-compartment pharmacokinetic model – was approximately 5 min, and took about 15 min for the signal to reach the noise level. It is important to note that the mouse heart rate is ~500 beats/min, compared with ~70 beats/min in humans; in this context, it is reasonable to assume that the circulation time of UW-17 would be significantly longer in humans. Furthermore, a 15-min circulation time is sufficient for blood pool imaging or angiography scans using real-time capable MPI scanners. In comparison, the MPS signal over time of Resovist did not fit the one-compartment pharmacokinetic model (Figure 8); as a result, its blood half-life pertaining to MPI was undefined. However, generally, Resovist demonstrated poor circulation characteristics – the MPS signal was considerably lower and nearly absent past 5 min of circulation. The increase in signal detected at 5 min suggests that the injected bolus takes 0–5 min for uniform distribution and is subsequently cleared from circulation.

Circulation time could likely be improved with further optimization of the MNP shell. The hydrodynamic size of formulation A was 86 nm (DLS Zavg), substantially larger than the magnetic core size of 17 nm. One potential cause of the larger hydrodynamic size is clustering of the magnetic particles after coating with polymer, which could lead to instability *in vivo*, and thus suboptimal circulation. Reducing hydrodynamic size to 30–50 nm, while maintaining colloidal stability in biological media, should prolong circulation time and enable use of ~25 nm MNPs, which show excellent MPI performance. Indeed, in the pilot biodistribution study, 37 nm hydrodynamic MNPs were cleared from the RES at least 2× slower than formulation A. Although formulation B's circulation time was still under investigation when this article went to press, the slower RES uptake provides indirect confirmation that it circulated longer.

Biodistribution and clearance

T2-weighted MRI of mice before and after MNP administration provided information on tissue distribution (Figure 9A). Similar to clinically approved superparamagnetic iron oxide agents, visual inspection suggests that our monodisperse MNPs distributed primarily in the liver and spleen – outlined yellow and red, respectively – post-MNP administration. Contrast analysis of T2-weighted images confirmed the latter; critically, there was minimal renal involvement (Figure 9B). Furthermore, the T2-weighted MRI contrast in the livers of mice injected with formulation A showed a gradual return to preinjection levels, suggesting a potential clearance pathway through the liver.

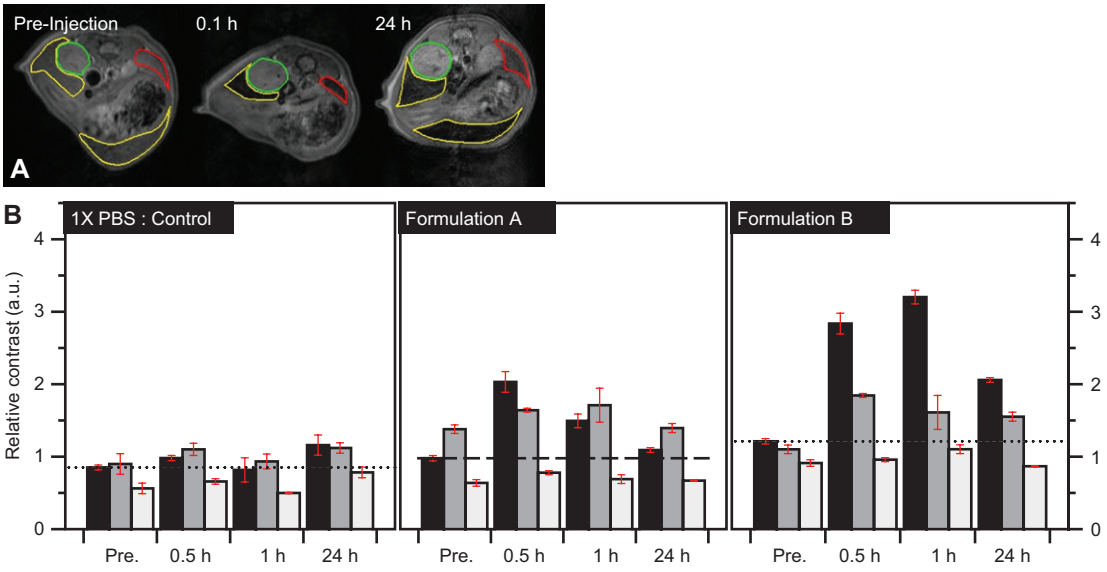

Figure 9 (A) T2-weighted images of mice preinjection, and 0.1 h and 24 h post-MNP administration, highlighting the liver (yellow), spleen (red), and kidney (green). (B) Biodistribution of MNPs with different hydrodynamic diameters, in the liver (black), spleen (gray) and kidney (white); formulation A (86 nm) is approximately twice the size of formulation B (37 nm). While both formulations predominantly distribute in the liver and spleen, with minimal renal involvement, A shows gradual clearance from liver about 0.5 h postinjection, whereas B continues to accumulate in liver 1 h postinjection. Note: the height of the relative contrast intensity is only qualitative and depends on both iron oxide concentration and T2-relaxivity (r2/mM Fe/s) of MNPs (see Table 2).

However, MRI contrast in the liver of mice injected with formulation B suggests that MNPs continued to accumulate 1 h postinjection. Clearance occurs between the 1 and 24 h imaging time points; thus, the precise onset is unclear. Critically, the smaller hydrodynamic diameter of formulation B contributes to slower RES uptake. Furthermore, it is especially promising that both formulations, after RES uptake, begin to clear through metabolic pathways in the liver and spleen. In this pilot safety study, the low-retention time demonstrated here is certainly promising; however, a comprehensive clearance study will involve radiolabeling all MNP components (core and shell) to monitor the eventual clearance of all tracer components.

Conclusions and outlook

For iron oxide MNP tracers used in MPI under standard conditions, the mechanism of magnetic reversal is predominantly Néel rotation of the moment within the magnetic crystal. However, we observed that MPI-tailored MNPs with sizes between 20 and 25 nm diameter are not superparamagnetic under these conditions; rather, their magnetic reversal is forced by the applied field, leading to hysteresis in the $m(H)$ response. We observed very little change in magnetic behavior measured by MPS when comparing an MNP sample that was dispersed in water and immobilized in gel, which confirms that the magnetic moment rotates without rotation of the particle. However, while Néel rotation is the dominant reversal mechanism, it is possible that the MNP anisotropy vectors align by small-angle Brownian rotation when the MNPs are dispersed in a liquid carrier.

Tuning the MNP energy barrier is the key to optimizing MPI response, as it determines the coercive field and the time rate of change of the moment under a given applied field. We have shown that controlling MNP size is an effective means of tuning performance, and that tuned MNPs can show submillimeter resolution in existing MPI scanners. Alternatively, the performance can also be improved by reducing the anisotropy constant, an approach that may be exploited in future developments of MPI tracers.

As viscous rotation contributes negligibly to MNP reversal under typical MPI conditions, the MNP shell can be designed to maximize *in vivo* stability and favorable pharmacokinetics. In early studies, we have seen that tuned MNPs circulate longer than Resovist, where the MPI signal intensity, measured by MPS, was used to determine circulation time. In more recent studies, we observed that uptake in the liver was slowed when the MNP coating was reduced from 86 to 37 nm (diameter). Measurements of

MNP biodistribution postinjection showed that clearance occurs through the RES system in the liver and spleen. Clearance time, like circulation, was affected by the polymer shell: in one formulation, clearance took place within 24 h, while in another, MNPs were still measured in liver and spleen tissue at 24 h. At no time was significant accumulation observed in the kidneys.

In conclusion, we have designed and synthesized biocompatible iron oxide MNPs tailored for MPI performance. Tailored MNPs showed increased linear resolution by a factor of 2 (or volume resolution by a factor of 8) compared with Resovist and improved SNR per unit tracer by a factor of 5. Results of *in vitro* studies show that performance is retained in biological media, and *in vivo* studies indicate good biocompatibility and biodistribution, suggesting that this approach is a promising way to optimize tracer performance for translational applications in biomedical imaging.

Acknowledgments: This work was supported by NIH grants 1R01EB013689-01/NIBIB and 1R41EB013520-01, NSF grant IIP-1215556, a UW/CGF commercialization grant and a Commercialization Fellowship (RMF).

Received January 30, 2013; accepted May 13, 2013

References

[1] Albanese A, Tang PS, Chan WCW. The effect of nanoparticle size, shape, and surface chemistry on biological systems. Annu Rev Biomed Eng 2012; 14: 1–16.
[2] Alexis F, Pridgen E, Molnar LK, Farokhzad OC. Factors affecting the clearance and biodistribution of polymeric nanoparticles. Mol Pharm 2008; 5: 505–515.
[3] Almeida JPM, Chen AL, Foster A, Drezek R. *In vivo* biodistribution of nanoparticles. Nanomedicine (Lond) 2011; 6: 815–835.
[4] Arami H, Krishnan KM. Highly stable amine functionalized iron oxide nanoparticles designed for magnetic particle imaging (MPI). IEEE Trans Magnet. 2013; 49(7).
[5] Arami H, Ferguson RM, Khandhar AP, Krishnan KM. Size-dependent ferrohydrodynamic relaxometry of magnetic particle imaging tracers in different environments. Med Phys 2012; 3: 267–268.
[6] Arami H, Stephen Z, Veiseh O, Zhang M. Chitosan-coated iron oxide nanoparticles for molecular imaging and drug delivery. In: Jayakumar R, Prabaharan M, Muzzarelli RAA, editors. Advances in polymer science, Chitosan for biomaterials I. Berlin: Springer 2011: 163–184.
[7] Bertotti G. Hysteresis in magnetism: for physicists, materials scientists, and engineers. 1st ed. San Diego, CA: Academic Press 1998.
[8] Biederer S, Sattel T, Knopp T, et al. A spectrometer to measure the usability of nanoparticles for magnetic particle imaging. In: Buzug TM, Borgert J, Knopp T, Biederer S, Sattel T, Erbe M, Lüdtke-Buzug K, editors. Magnetic nanoparticles: particle science, imaging technology, and clinical applications. Singapore: World Scientific 2010: 60–65.
[9] Carrey J, Mehdaoui B, Respaud M. Simple models for dynamic hysteresis loop calculations of magnetic single-domain nanoparticles: application to magnetic hyperthermia optimization. J Appl Phys 2011; 109: 083921.
[10] Chikazumi S. Physics of magnetism. New York: Wiley 1964.
[11] Cole AJ, David AE, Wang J, Galbán CJ, Hill HL, Yang VC. Polyethylene glycol modified, cross-linked starch-coated iron oxide nanoparticles for enhanced magnetic tumor targeting. Biomaterials 2011; 32: 2183–2193.
[12] Eberbeck D, Wiekhorst F, Wagner S, Trahms L. How the size distribution of magnetic nanoparticles determines their magnetic particle imaging performance. Appl Phys Lett 2011; 98: 182502.
[13] Ferguson RM, Khandhar AP, Krishnan KM. Tracer design for magnetic particle imaging (invited). J Appl Phys 2012; 111: 07B318.
[14] Ferguson RM, Minard KR, Khandhar AP, Krishnan KM. Optimizing magnetite nanoparticles for mass sensitivity in magnetic particle imaging. Med Phys 2011; 38: 1619–1626.
[15] Frenkel J. Kinetic theory of liquids. New York: Dover 1955.
[16] Gleich B, Weizenecker J. Tomographic imaging using the nonlinear response of magnetic particles. Nature 2005; 435: 1214–1217.
[17] Goodwill PW, Conolly SM. The X-space formulation of the magnetic particle imaging process: 1-D signal, resolution, bandwidth, SNR, SAR, and magnetostimulation. IEEE Trans Med Imaging 2010; 29: 1851–1859.
[18] Goodwill P, Conolly S. Multidimensional X-space magnetic particle imaging. IEEE Trans Med Imaging 2011; 30: 1581–1590.
[19] Goodwill PW, Saritas EU, Croft LR, et al. X-space MPI: magnetic nanoparticles for safe medical imaging. Adv Mater 2012; 24: 3870–3877.
[20] Goodwill PW, Tamrazian A, Croft LR, et al. Ferrohydrodynamic relaxometry for magnetic particle imaging. Appl Phys Lett 2011; 98: 262502–262502.
[21] Hua L, Ferguson RM, Hovorka O, Chantrell RW, Krishnan KM. Simulations of MPI tracer performance using a kinetic Monte Carlo method. Proceedings of International Workshop on magnetic particle imaging 2013. IEEE Xplore. Accepted for publication
[22] Huong NT, Giang LTK, Binh NT, Minh LQ. Surface modification of iron oxide nanoparticles and their conjugation with water soluble polymers for biomedical application. J Phys Conf Ser 2009; 187: 012046.
[23] Khandhar AP, Ferguson RM, Arami H, Krishnan KM. Monodisperse magnetite nanoparticle tracers for *in vivo* magnetic particle imaging. Biomaterials 2013; 34: 3837–3845.

[24] Khandhar AP, Ferguson RM, Simon JA, Krishnan KM. Tailored magnetic nanoparticles for optimizing magnetic fluid hyperthermia. J Biomed Mater Res A 2012; 100: 728–737.
[25] Krishnan KM. Biomedical nanomagnetics: a spin through possibilities in imaging, diagnostics, and therapy. IEEE Trans Magn 2010; 46: 2523–2558.
[26] Löwa N, Eberbeck D, Steinhoff U, Wiekhorst F, Trahms L. Potential of improving MPI performance by magnetic separation. In: Buzug TM, Borgert J, editors. Springer proceedings in physics. Berlin: Springer 2012: 73–78.
[27] Lu M, Cohen MH, Rieves D, Pazdur R. FDA report: ferumoxytol for intravenous iron therapy in adult patients with chronic kidney disease. Am J Hematol 2010; 85: 315–319.
[28] Narayanan J, Xiong J-Y, Liu X-Y. Determination of agarose gel pore size: absorbance measurements vis a vis other techniques. J Phys: Conf Ser 2006; 28: 83–86.
[29] Rahmer J, Weizenecker J, Gleich B, Borgert J. Signal encoding in magnetic particle imaging: properties of the system function. BMC Med Imaging 2009; 9: 4.
[30] Rahmer J, Weizenecker J, Gleich B, Borgert J. Analysis of a 3-D system function measured for magnetic particle imaging. IEEE Trans Med Imaging 2012; 31: 1289–1299.
[31] Reimer P, Balzer T. Ferucarbotran (Resovist): a new clinically approved RES-specific contrast agent for contrast-enhanced MRI of the liver: properties, clinical development, and applications. Eur Radiol 2003; 13: 1266–1276.
[32] Sarin H. Physiologic upper limits of pore size of different blood capillary types and another perspective on the dual pore theory of microvascular permeability. J Angiogenes Res 2010; 2: 14.
[33] Schmale I, Rhamer J, Gleich B, Borgert J, Weizenecker J. Point spread function analysis of magnetic particles. In: Buzug TM, Borgert J, editors. Magnetic particle imaging, Springer proceedings in physics 140. Berlin: Springer-Verlag 2012: 287–292.
[34] Shliomis MI. Magnetic fluids. Soviet Physics Uspekhi 1974; 17: 153–169.
[35] Stoner EC, Wohlfarth EP. A mechanism of magnetic hysteresis in heterogeneous alloys. Philos Trans R Soc Lond Ser A Math Phys Sci 1948; 240: 599–642.
[36] Usov NA, Liubimov BY. Dynamics of magnetic nanoparticle in a viscous liquid: application to magnetic nanoparticle hyperthermia. J Appl Phys 2012; 112: 023901.
[37] Weissleder R, Elizondo G, Wittenberg J, Rabito CA, Bengele HH, Josephson L. Ultrasmall superparamagnetic iron-oxide – characterization of a new class of contrast agents for MR imaging. Radiology 1990; 175: 489–493.
[38] Weissleder R, Stark DD, Engelstad BL, et al. Superparamagnetic iron oxide: pharmacokinetics and toxicity. AJR Am J Roentgenol 1989; 152: 167.
[39] Weizenecker J, Gleich B, Rahmer J, Dahnke H, Borgert J. Three-dimensional real-time *in vivo* magnetic particle imaging. Phys Med Biol 2009; 54: L1–L10.
[40] Weizenecker J, Gleich B, Rahmer J, Borgert J. Micro-magnetic simulation study on the magnetic particle imaging performance of anisotropic mono-domain particles. Phys Med Biol 2012; 57: 7317–7327.
[41] Wen T, Krishnan KM. Cobalt-based magnetic nanocomposites: fabrication, fundamentals and applications. J Phys D Appl Phys 2011; 44: 393001.